Multivariate statistical air mass classification for the high-alpine observatory at the Zugspitze mountain, Germany

Armin Sigmund[1,*], Korbinian Freier[2,3], Till Rehm[4], Ludwig Ries[5], Christian Schunk[6,+], Anette Menzel[6,7], and Christoph K. Thomas[1]

[1]Micrometeorology Group, University of Bayreuth, Bayreuth, Germany
[2]Bavarian Environment Agency, Augsburg, Germany
[3]Research Unit Sustainability and Global Change, Center for Earth System Research and Sustainability (CEN), University of Hamburg, Hamburg, Germany
[4]Environmental Research Station Schneefernerhaus, Zugspitze, Germany
[5]German Environment Agency, GAW Global Observatory, Zugspitze-Hohenpeissenberg, Germany
[6]Ecoclimatology, Technical University of Munich, Freising, Germany
[7]Institute for Advanced Study, Technical University of Munich, Garching, Germany
[*]now at: School of Architecture, Civil and Environmental Engineering, Swiss Federal Institute of Technology, Lausanne, Switzerland
[+]now at: Safety and Radiation Protection, Technical University of Munich, Garching, Germany
Correspondence: A. Sigmund (armin.sigmund@epfl.ch)

Abstract. To assist atmospheric monitoring at high-alpine sites, a statistical approach for distinguishing between the dominant air masses was developed. This approach was based on a principal component analysis using five gas-phase and two meteorological variables. The analysis focused on the site Schneefernerhaus at Mt. Zugspitze, Germany. The investigated year was divided into 2-month periods, for which the analysis was repeated. Using the 33.3 % and 66.6 % percentiles of the first two principal components, nine air mass regimes were defined. These regimes were interpreted with respect to vertical transport and assigned to the air mass classes BL (recent contact with the boundary layer), UFT/SIN (undisturbed free troposphere or stratospheric intrusion), and HYBRID (influences of both the boundary layer and the free troposphere or ambiguous). The input data were available in 78 % of the investigated year. BL accounted for 31 % of the cases with similar frequencies in all seasons. UFT/SIN comprised 14 % of the cases but was not found from April to July. HYBRID (55 %) mostly exhibited intermediate characteristics, whereby 17 % of HYBRID suggested an influence of the marine boundary layer or the lower free troposphere. The statistical approach was compared to a mechanistic approach using the ceilometer-based mixing layer height from a nearby valley site and a detection scheme for thermally induced mountain winds. Due to data gaps, only 25 % of the cases could be classified with the mechanistic approach. Both approaches agreed well, except in the rare cases of thermally induced uplift. The statistical approach is a promising step towards a real-time classification of air masses. Future work is necessary to assess the uncertainty arising from the standardization of real-time data.

1

1 Introduction

High-alpine observatories such as the Environmental Research Station Schneefernerhaus (UFS) at Mt. Zugspitze, Germany, play an important role in studying changing concentrations of atmospheric constituents such as greenhouse gases, aerosols, and persistent organic pollutants (POPs), which have critical impacts on the climate, environmental integrity, or human health (McClure et al., 2016; Kirchner et al., 2016). In particular, high-alpine observatories frequently offer the opportunity to sample well-mixed air masses of the free troposphere. These air masses are representative for large spatial areas and thus suitable for the determination of large-scale and global trends (Yuan et al., 2019). Therefore, the observational network of the Global Atmosphere Watch Program of the World Meteorological Organization includes many high-alpine observatories. At times, however, high-alpine sites can be affected by local anthropogenic emissions on the mountain or regional emissions if air masses of the boundary (BL) are lifted or mixed with the free troposphere by processes such as synoptic lifting (e.g. at fronts), thermally induced anabatic winds, and foehn flows (Zellweger et al., 2003). Foehn winds descend on the lee side of a mountain range and can be associated with air mass lifting on the windward side. In relatively rare cases, the air masses at high-alpine sites originate from the stratosphere, e.g. on approximately 6 % of the days at Mt. Zugspitze (Stohl et al., 2000).

The BL can be defined "as the part of the troposphere that is directly influenced by the presence of the earth's surface, and responds to surface forcings with a time scale of about an hour or less" (Stull, 1988). Reuten et al. (2007) proposed to use a time scale of one diurnal cycle for this definition to explicitly include the residual layer above a stably stratified nocturnal boundary layer and elevated aerosol layers that can result from thermally driven upslope flows (Gohm et al., 2009). For instance, on typical fair weather days in summer, Henne et al. (2004) observed a two-layer structure of the BL in deep Alpine valleys where upslope flows lifted air from a polluted lower layer to a moderately polluted injection layer that reached well above the crest height.

In air pollution studies, the terms mixing layer or mixed layer are more common than BL and were defined as "the layer adjacent to the ground over which pollutants or any constituents emitted within this layer or entrained into it become vertically dispersed by convection or mechanical turbulence within a time scale of about an hour" (Seibert et al., 2000). Over flat terrain, the mixing layer typically coincides with the BL, at least during daytime. Following Reuten et al. (2007), we use a time scale of one diurnal cycle and consider a residual layer and elevated aerosol layers as parts of the BL and the mixing layer.

Basically, there are two different approaches for air mass classification at high-alpine sites. Mechanistic approaches investigate directly atmospheric transport processes using meteorological measurements or trajectory models, whereas statistical approaches infer the influences of the air layers from the air mass composition at the site and, possibly, meteorological auxiliary data.

Zellweger et al. (2003) used a mixed mechanistic and statistical approach at the high-alpine site Jungfraujoch, Switzerland. They identified three transport processes, namely foehn events, synoptical lifting, and thermally induced uplift, and attributed the other cases to the undisturbed free troposphere. Foehn events and synoptic lifting were detected with mechanistic approaches using standard meteorological measurements and the height of back-trajectories, respectively. Thermally induced

uplift was determined with a statistical approach based on the diurnal variation of the sum of oxidized nitrogen species (NO_y) or, in the case of data gaps, the aerosol surface area concentration or specific humidity.

In a recent study, Hulin et al. (2019) explored different methods for selecting days with thermally driven circulations influencing the Pic du Midi high-alpine observatory in the French Pyrenees. A statistical method based on the diurnal cycle of specific humidity seemed to be most reliable. Wind profiler measurements above the nearby plain indicated that a plain-mountain circulation with an upper-level return-flow played an important role although this circulation was sometimes not visible in the near-surface in-situ wind measurements in the plain.

Other studies used a ground-based lidar or ceilometer that was installed near a high-alpine site at a lower altitude to determine the mixing layer height (MLH) from the vertical aerosol backscatter profile (Gallagher et al., 2012; Ketterer et al., 2014). This method is considered as a mechanistic approach because the determination of the MLH from vertical profiles of measured quantities requires a-priori meteorological knowledge. Recently, Poltera et al. (2017) used a tilted configuration of a ceilometer and demonstrated that the Jungfraujoch was rarely embedded in the local convective boundary layer but much more frequently in an above lying injection layer with slightly higher aerosol concentrations compared to the free troposphere.

Some statistical approaches defined a threshold for the concentration of a surface-emitted atmospheric constituent or a ratio of constituents. At the Mt. Bachelor Observatory, USA, a seasonal or monthly threshold for the water vapor mixing ratio was used to distinguish between free-tropospheric and BL influenced air masses (Ambrose et al., 2011; Zhang and Jaffe, 2017). The threshold was chosen such that the water vapor mixing ratios below this threshold had the same seasonal or monthly mean as the data from National Weather Service soundings that were launched at a lower elevated site.

For the Jungfraujoch, Herrmann et al. (2015) compared a mechanistic approach, which was based on back-trajectories and an inventory of carbon monoxide (CO) emissions, with two simple statistical approaches that used a constant threshold of the radon-222 concentration and the ratio of CO to NO_y. The CO/NO_y threshold appeared to achieve the best distinction between free-tropospheric and BL influenced air masses but the authors noted that a single threshold cannot account for varying degrees of BL influence (Herrmann et al., 2015).

Other statistical approaches aimed at selecting baseline (also called background) concentrations of a trace gas at different kinds of remote sites and were based on outlier removal techniques (e.g. Ruckstuhl et al., 2012) or the fact that well-mixed air masses result in a small temporal variability of the trace gas mixing ratio (e.g. Yuan et al., 2018). Baseline concentrations refer to a given species in a well-mixed air mass with a minimal influence of anthropogenic impurities of relatively short lifetime (Calvert, 1990; Yuan et al., 2018), which is associated with the free troposphere at high-alpine sites.

In contrast to mechanistic approaches, statistical air mass classifications are not able to distinguish between different uplift processes but require only local data. So far, however, statistical approaches were only based on a single constituent or a ratio of constituents, although several atmospheric constituents are typically monitored at high-alpine observatories.

This study proposes a novel statistical approach based on a principal component analysis (PCA) using seven chemical and meteorological variables. This approach is intended for a later use in real-time operational mode to enable an automated sampling of ambient air with respect to different air masses using a multi-channel sampling system for monitoring of POPs (Kirchner et al., 2016). The objectives were to (i) develop a statistical classification scheme for the site UFS at Mt. Zugspitze and

to (ii) validate this approach, as far as possible, with a mechanistic approach based on ceilometer and standard meteorological measurements.

2 Methods

2.1 Measurement sites

The UFS (47°25'00" N, 10°58'47" E, 2650 m a.s.l.) is located on a steep south-facing slope, approximately 300 m below the summit of Mt. Zugspitze (2962 m a.s.l.), which is the highest mountain in the German Alps and represents the first real barrier for northwesterly advection from the Alpine foreland. At the UFS, westerly and easterly wind directions dominate due to the local topography (Risius et al., 2015). Because of trace gas and aerosol measurements, the UFS reduced its emissions of these substances to a minimum. Nevertheless, the measurements can be influenced by local emissions from the direct surrounding, which is a highly frequented tourist area all year round. Local emission sources include nearby cable car stations at the Zugspitze summit (ZSG) and the Zugspitzplatt (ZPLT) which is a gently sloping plateau below the UFS (Fig. 1). Additionally, a skiing area is situated at the ZPLT. The large metropolitan area of Munich is approximately 90 km north of the study site.

Beside the UFS, seven weather stations at different altitudes at a maximum horizontal distance of 11 km from the UFS were available and included in this study (Fig. 1). One of these stations is located at ZSG. Another weather station is located on the ZPLT which is surrounded by mountain ridges except towards the east where the plateau leads to the narrow and deep valley Reintal. The weather stations Schachen (1830 m a.s.l.), Kreuzalm (1600 m a.s.l.), Felsenkanzel (1250 m a.s.l.), and Brandwiese (900 m a.s.l.) are part of the project KLIMAGRAD (Schuster et al., 2014). The site Schachen is situated on a plateau above the middle Reintal in close vicinity of some trees. Kreuzalm is situated on a meadow on a mountain saddle. Brandwiese is located on a meadow surrounded by forest, where a tributary valley reaches the Reintal from the west. At Felsenkanzel, the measurements are made on a steep south-facing slope northwest of the town of Garmisch-Partenkirchen (GAP). The site GAP (720 m a.s.l) is located in the western periphery of the town where a broad west-east oriented valley turns to northeast towards the alpine foreland (Fig. 1).

2.2 Instrumentation and data set

The data set that was analyzed in this study spans a period of 1 year from 22 August 2013 to 21 August 2014, which was selected for high data availability. Table 1 gives an overview of the chemical measurements, associated instruments, measurement principles, and research institutions that provided the data. Most of the atmospheric constituents are measured at the UFS, including carbon mono- (CO) and dioxide (CO_2), methane (CH_4), ozone (O_3), the sum of oxidized nitrogen species (NO_y), nitrogen oxides ($NO_x = NO + NO_2$ with NO and NO_2 being nitrogen mono- and dioxide, respectively), formaldehyde (HCHO), the ambient particle number size distribution ($dN\,(dlog\,d_p)^{-1}$) for particle diameters (d_p) between 10 nm and 600 nm, the mass concentration of particulate matter with $d_p < 10$ μm (PM_{10}), and equivalent black carbon (eBC). The

radioisotopes beryllium-7 (^{7}Be) and radon-222 (^{222}Rn) are sampled at ZSG and the mountain ridge (2825 m a.s.l.) directly above the UFS, respectively. At the remaining sites, only meteorological parameters are recorded.

While most of the chemical data were available as 1 min averages, HCHO and the particle size distribution were provided at 10 min intervals and ^{222}Rn and ^{7}Be were available as 2 h and 12 h averages, respectively (Table 1). The HCHO data contained a large data gap between 15 December 2013 and 15 July 2014 and the ^{222}Rn data was only available since 1 January 2014. The ^{222}Rn data were downloaded from the World Data Centre for Greenhouse Gases (WDCGG, 2019). Because ^{7}Be attaches to aerosol particles, it is measured by collecting the carrier aerosol with a glass fiber filter. While NO can be measured directly, NO_y and NO_2 have to be converted to NO before the detection. This conversion of NO_y and NO_2 is performed with photolysis and gold/CO converters, respectively.

The standard meteorological measurements included air temperature (T), relative humidity (rH), global radiation (R_g), and horizontal wind velocity and direction at all sites. Air pressure (p) was available at the sites UFS, ZSG, and GAP. Additionally, year-round precipitation measurements with an electronic weighing system and a windbreak ring (Sommer Messtechnik, Koblach, Austria) at the site ZPLT were used. At the ZPLT and the four KLIMAGRAD sites, the wind data is measured by propeller anemometers (Wind Monitor 05103, Young, Traverse City, USA) while at GAP and ZSG, cup anemometers and wind vanes (SK-565 and SK-566, respectively, Thies Clima, Göttingen, Germany) are used. At the UFS, an ultrasonic anemometer (model 2D, Thies Clima, Göttingen, Germany) is used. The standard meteorological data were available as 10 min averages except at the UFS (1 min averages).

At GAP, a ceilometer (CHM 15k, Lufft, Fellbach, Germany) provides 15 s averages of up to three aerosol layer heights (ALHs) with a vertical resolution of 15 m using a wavelet algorithm of the manufacturer, which detects strong gradients in the range corrected attenuated backscatter profile. In the absence of clouds, the signal-to-noise ratio of the ceilometer is typically > 1 up to a height of 4 to 5 km a.g.l. in the daytime and up to greater heights at night (Heese et al., 2010).

2.3 Data post-processing and quality control

All time stamps were converted to local standard time. The data were aggregated on a 30 min basis while requiring a data availability of $\geq 66\%$ in each interval unless stated differently. The ^{222}Rn and ^{7}Be concentrations were interpolated using nearest neighbor interpolation to match them with the 30 min intervals used for the analysis.

2.3.1 Atmospheric constituents

The chemical measurements were quality controlled by the research institutions that provided the data. Invalid data, which resulted from calibration, instrument repair, or power failure, were discarded.

Due to measurement uncertainties, NO_y occasionally exhibited a lower mixing ratio than NO_x. If NO_y was lower than 75 % of NO_x and NO_x was at least 0.03 ppb, both quantities were treated as artifacts and were discarded. If NO_y remained still lower than NO_x after averaging on a 30 min basis, both quantities were assumed to be equal and were replaced by the mean of NO_x and NO_y. Negative eBC concentrations were treated in a similar way. Values below $-0.05\,\mu g\,m^{-3}$ were discarded. If eBC remained still negative after averaging on a 30 min basis, the concentration was set to zero.

The processing of the particle number size distributions is described in Birmili et al. (2016) and includes, among others, a multiple charge inversion and corrections for particle losses. Following Herrmann et al. (2015), the number concentration of accumulation mode particles (N_{90}) was used as an indicator for BL air masses and approximated by including particle diameters between 90 nm and 600 nm.

Data of most trace gases and PM_{10} had been flagged manually with respect to locally polluted air masses. These air masses are a special kind of BL air masses because they do not result from uplift processes but from human activities on the mountain. Local emissions were evident from short but pronounced peaks in trace gas and aerosol concentrations and were most frequently observed for NO_x and NO_y. The flag for local NO_x emissions was approximately reproduced by selecting data with a 30 min NO_x standard deviation (σ_{NO_x}) of > 0.4 ppb (not shown). According to this criterion, local pollution events affected 9 % of the NO_x data but half of these events lasted no longer than one time interval, i.e. 30 min. Consequently, local pollution events are generally so short that they cannot be predicted on a 30 min basis in real-time applications. Therefore and because the classification scheme was developed for a later use in real-time operational mode, the air mass classification does not account for local pollution events.

2.3.2 Standard meteorological data

The wind data at ZSG and GAP were discarded for wind velocities below the starting threshold of the wind vane of $0.3\,\mathrm{m\,s^{-1}}$ for a displacement of $90°$ (Löffler, 2012). For the wind vane of the propeller anemometers at the ZPLT and the KLIMAGRAD sites, the starting threshold was $1.1\,\mathrm{m\,s^{-1}}$ (Young, 2018). To achieve a trade-off between a high data quality and a high data availability, the wind data of these anemometers were discarded for wind velocities of $< 0.7\,\mathrm{m\,s^{-1}}$.

The standard meteorological data were aggregated on a 30 min basis using the vector mean for wind direction, the sum for precipitation, and the arithmetic mean for the other variables. Specific humidity q $(\mathrm{g\,kg^{-1}})$ and virtual potential temperature θ_v (K) were calculated for each site as follows (Foken, 2008),

$$q = 0.622\,\frac{e}{p - 0.378\,e} \tag{1}$$

$$\theta_v = (1 + 0.608\,q)\,T\left(\frac{p_0}{p}\right)^{R_L/c_p}, \tag{2}$$

where e (hPa) is vapor pressure, p (hPa) is air pressure, p_0 is 1000 hPa, T (K) is air temperature, R_L $(\mathrm{J\,kg^{-1}\,K^{-1}})$ is the gas constant of dry air, and c_p $(\mathrm{J\,kg^{-1}\,K^{-1}})$ is specific heat capacity of dry air. The vapor pressure was calculated from relative humidity (rH) and T using the Clausius Clapeyron equation. Because p was only measured at the sites ZSG, UFS, and GAP, it was calculated for the other sites using the hypsometric equation,

$$p = p_{ref} \exp\left\{-\frac{g_0\,(Z - Z_{ref})}{R_L\,\overline{T}_v}\right\}, \tag{3}$$

where p (hPa) and p_{ref} (hPa) are the air pressures at the site of interest and a reference site, respectively, Z (m) and Z_{ref} (m) are the geopotential heights that were approximated with the altitudes of the respective sites, g_0 is $9.8\,\mathrm{m\,s^{-2}}$, R_L $(\mathrm{J\,kg^{-1}\,K^{-1}})$

is the gas constant of dry air, and $\overline{T}_v$ (K) is the mean virtual temperature for the air layer between the two sites under consideration. p was computed in two steps. First, p was approximated using the dry-bulb temperature instead of $\overline{T}_v$. Second, $\overline{T}_v$ was calculated with the approximated p and used to recalculate p. The UFS was used as the reference site to calculate p at the next lower site (ZPLT), which was afterwards used as the reference site to calculate p at the next lower site (Schachen). This procedure was continued until Kreuzalm. Similarly, GAP was used as the reference site to determine p at the next higher site and this procedure was continued until Schachen. At Kreuzalm and Schachen, the two p estimates based on the next lower and next higher sites were averaged.

In order characterize the static stability of the valley atmosphere with a single quantity, the range of the pseudo-vertical profile of virtual potential temperature ($\Delta\theta_v$ (K)) was defined as follows, considering all stations except Schachen,

$$\Delta\theta_v = \begin{cases} \theta_v^{\max} - \theta_v^{\min}, & \text{if } z_{\theta_v^{\min}} \leq z_{\theta_v^{\max}} \\ \theta_v^{\min} - \theta_v^{\max}, & \text{if } z_{\theta_v^{\min}} > z_{\theta_v^{\max}}, \end{cases} \tag{4}$$

where $\theta_v^{\min}$ (K) and $\theta_v^{\max}$ (K) are minimum and maximum virtual potential temperature of the pseudo-vertical profile, respectively, and $z_{\theta_v^{\min}}$ (m) and $z_{\theta_v^{\max}}$ (m) are the associated altitudes. Schachen was excluded from this calculation because θ_v was particularly high at Schachen if the global radiation was high and the wind velocity was low, which suggested that the naturally aspirated thermometer was affected by radiative errors (not shown). $\theta_v^{\min}$ was mostly found at the low-elevation sites GAP and Brandwiese, which applied to 58 % and 37 % of the cases, respectively. $\theta_v^{\max}$ occurred mostly at the high-elevation sites ZSG, UFS, or ZPLT, which applied to 68 %, 18 %, and 13 % of the cases, respectively. The values of $\Delta\theta_v$ ranged between -5 K and $+31$ K, where positive values indicate stable conditions (see supplement, Fig. S1a).

2.3.3 Ceilometer data

To determine the MLH at GAP from the ALH retrievals of the ceilometer, several post-processing steps were necessary (Fig. 2). ALHs below 600 m a.g.l., corresponding to 1320 m a.s.l., were regarded as artifacts and were discarded because of high measurement uncertainties in this part of the backscatter profile resulting from an incomplete overlap of the laser beam and the field of view of the ceilometer (Flentje et al., 2010). The backscatter signal only reflects aerosol concentrations below clouds. Thus, ALHs that were greater or equal to the cloud base height, which was measured by the same instrument, were discarded. For this reason, it was not possible to determine the correct MLH if clouds were present at the top of or within the mixing layer. These first two post-processing steps strongly reduced the data availability from 89 % to 45 % of the time.

If two or three ALHs were found at the same time, the following procedure was applied. For each ALH, the number of ALHs in its vicinity, i.e. within centered intervals of 300 m and 30 min in the vertical and temporal dimensions, respectively, was determined. The ALH with the maximum number of ALHs in its vicinity was attributed to the MLH while the other ALHs were discarded. If each of the ALHs had less than three ALHs in its vicinity, a missing value was registered. The MLH attribution, as described above, was based on the idea that the MLH varies only gradually so that similar MLHs are expected shortly before and after the time under consideration. In particular situations, in which elevated aerosol layers enter or leave the field of view of the ceilometer, this assumption may not be valid.

From the resulting time series at 15 s intervals, outliers were removed iteratively as follows. From each pair of subsequent data points with an absolute rate of change exceeding $240\ \mathrm{m\ min^{-1}}$, one data point was removed so that the standard deviation of the MLH in the preceeding 15 min and the following 15 min was most strongly reduced. This procedure was repeated until the absolute rate of change was maximum $240\ \mathrm{m\ min^{-1}}$ corresponding to four vertical averaging intervals $(4 \cdot 15\ \mathrm{m})$ per time interval (15 s).

The MLHs were aggregated using the 30 min median while requiring a data availability of $\geq 50\ \%$ and a standard deviation of $\leq 170\ \mathrm{m}$ corresponding to the 90 % percentile of all 30 min standard deviations. From the aggregated time series, outliers were removed in the same way as described above but with a maximum allowed absolute rate of change of $400\ \mathrm{m\ h^{-1}}$. Finally, the MLH was available for 34 % of the time.

2.4 Statistical classification approach

2.4.1 Definition of the air mass classes

The statistical analysis aimed at distinguishing the following three classes of air masses: (a) BL: Air masses with a recent contact with the BL, characterized by increased concentrations of surface-emitted atmospheric constituents suggesting a recent uplift with a dominating influence of regional or local sources; (b) UFT/SIN: Air masses of the undisturbed free troposphere or stratospheric intrusions, characterized by very low concentrations of surface-emitted constituents suggesting recent subsidence or horizontal advection; and (c) HYBRID: Air masses that are influenced by both the BL and the free troposphere or that exhibit ambiguous characteristics. The class HYBRID was anticipated, for example, if the air mass had been exported from the BL to the free troposphere at a significant horizontal distance from the UFS and had been mixed with the free troposphere on the further trajectory, resulting in intermediate concentrations of surface-emitted constituents.

Stratospheric intrusions are characterized by high $^7\mathrm{Be}$ and $\mathrm{O_3}$ concentrations and a low humidity and have been observed at Mt. Zugpitze on approximately 5 % of the days (Stohl et al., 2000). Because of this low frequency and the coarse temporal resolution of $^7\mathrm{Be}$ of 12 h, stratospheric intrusions were not classified individually but attributed to the same class as air masses of the undisturbed free troposphere, which exhibit similar characteristics.

2.4.2 Principal component analysis

A PCA allows for reducing the number of dimensions of a data set while maintaining as much variance as possible. Principal components (PCs) are uncorrelated standardized linear combinations of the original variables (Mardia et al., 1979). If the variance of the original variables is mainly caused by shifts between the air mass classes, the first few PCs will be suitable indicators for air mass classification. The PCA was performed separately for 2-month periods to (i) account for seasonally changing relationships between the variables and to (ii) largely eliminate the influence of the seasonal variability of atmospheric constituents because the seasonality reflects not only the frequency of BL influenced air masses but also other factors such as the source and sink strength (e.g. residential heating in winter, photosynthetic $\mathrm{CO_2}$ removal in summer), chemical reactivity, and deposition. The original variables were standardized by subtracting the arithmetic mean and dividing by the standard

deviation of the respective 2-month period in order to avoid biased results due to different units and ranges of the data. The subtraction of the 2-month mean roughly removes the seasonal cycle.

Only variables with an expected unambiguous link to vertical transport processes and a high data availability were used as input variables of the PCA. These variables include the gases CO, CH_4, CO_2, O_3, and water vapor. Among the meteorological variables, the air pressure at GAP and $\Delta\theta_v$ were considered most suitable for the PCA because they are physically linked to uplift (low pressure, low static stability) and subsidence processes (high pressure, high static stability). The remaining variables were only used for validation purposes. Aerosol measurements were excluded from the PCA because low aerosol concentrations do not necessarily indicate UFT/SIN air masses but can also result from wet deposition during the uplift of BL air masses. ^{222}Rn and HCHO were only used for validation purposes due to low data availability. NO_y and NO_x were excluded from the PCA because their variability was particularly strongly influenced by local emissions, which are not indicative of uplift processes. O_3 was only used as PCA input variable in the winter half year because high O_3 mixing ratios are not only caused by a subsidence of UFT/SIN air masses but can also result from photochemical O_3 production in BL air masses, which typically contain high precursor concentrations. In the winter half year, photochemical O_3 production was assumed to play a minor role at high-alpine sites because of the generally low solar irradiance and the weak thermally induced uplift. This argument is supported by trajectory residence time statistics of Kaiser et al. (2007), which demonstrated that in winter, the O_3 mixing ratio at European high-alpine sites was generally lower if the air mass originated from lower altitudes, whereas in summer, this was often not the case.

The 2-month periods were defined as December to January, February to March, . . . , so that the winter and summer half years included the months with the lowest and highest solar forcing, respectively. The PCs were computed from the following five gas-phase variables and two meteorological variables, where O_3 was only included in the 2-month periods of the winter half year (October to March),

$$\mathrm{PC}_i = a_{1i}\widehat{[CO]} + a_{2i}\widehat{[CH_4]} + a_{3i}\widehat{[CO_2]} + a_{4i}\widehat{[O_3]} + a_{5i}\widehat{q} + a_{6i}\widehat{\Delta\theta_v} + a_{7i}\widehat{p_{GAP}} \ . \tag{5}$$

Here, PC_i represents the scores of the i-th PC; $\widehat{[CO]}, \widehat{[CH_4]}, \widehat{[CO_2]}$, and $\widehat{[O_3]}$ are the standardized mixing ratios of the respective trace gases at the UFS; $\widehat{q}$ is the standardized specific humidity at the UFS; $\widehat{\Delta\theta_v}$ is the standardized range of the pseudo-vertical profile of virtual potential temperature; $\widehat{p_{GAP}}$ is the standardized air pressure at GAP; and $a_{1i}, \ldots, a_{7i}$ are the loadings of the i-th PC. All quantities in Eq. 5 are dimensionless due to standardization. The loadings represent standardized eigenvectors of the correlation matrix of the original variables while the associated eigenvalues correspond to the variances of the PC scores (Mardia et al., 1979).

2.4.3   Isolating regimes and classes of air masses

In each 2-month period, the air masses were divided into nine regimes using the 33.3 % and 66.6 % percentiles of the first two PCs as thresholds (Fig. 3). The division of each of the two PCs into three equally large subsets follows the same logic as the definition of the three air mass regimes. ML and UFT/SIN air masses are expected on opposite edges of the distributions of the PC1 and PC2 scores while a mixture of these air masses may be found in the middle part of the distributions. The nine regimes

were interpreted with respect to vertical transport and attributed to the three air mass classes BL, UFT/SIN, and HYBRID by visually comparing summary statistics of the PCA input variables between the regimes. In the winter half year, the regimes were assigned to the class BL if CO, CH_4, CO_2, and q were relatively high and $\Delta\theta_v$, p_{GAP} and O_3 were relatively low compared to the other regimes. The class UFT/SIN was assigned in the opposite case and the remaining regimes were assigned to the class HYBRID. Apart from CO_2 and O_3, the same criteria were used in the summer half year. Due to photosynthesis, CO_2 was required to be relatively low for BL air masses compared to other air masses during the summer half year. O_3 was not used as an input variable in the summer half year.

This subjective mapping of regimes to classes of air masses was validated using summary statistics of the remaining chemical (e.g. NO_y, NO_x, ^{222}Rn) and standard meteorological measurements (e.g. precipitation, relative humidity). Long-range transport of mineral dust (LRMD) was regarded as a subclass of HYBRID and was identified with the following three criteria: (i) a high PM_{10} concentration of $\geq 13\,\mu g\,m^{-3}$, (ii) a relatively low $30\,min$ standard deviation of the PM_{10} of $\leq 0.2\,PM_{10}$ to avoid the attribution of local pollution events, and (iii) an air mass regime that does not suggest a current uplift of BL air masses. The PM_{10} threshold of $13\,\mu g\,m^{-3}$ was motivated by a local minimum in the PM_{10} histogram for non-BL air masses in June–July (not shown) and the plausibility was checked by visual inspection of the whole PM_{10} time series. Ambiguous air mass regimes, which carried the fingerprint of the marine boundary layer or the lower free troposphere (among others, very low CO and CH_4 mixing ratios but high q and low O_3 mixing ratios) were attributed to MBL/UFT, another subclass of HYBRID, unless the criteria for LRMD were fulfilled (Fig. 3). Characteristics of the marine boundary layer can be observed in the Alps if the air mass was lifted above the Atlantic Ocean and transported to the Alps within several days (Balzani Lööv et al., 2008).

2.5 Mechanistic classification approach

In search of criteria for thermally induced anabatic and katabatic winds that influence the UFS, the wind directions of all sites were investigated. The wind direction at the UFS was not useful because upslope and downslope flows were not clearly visible but appeared to be superimposed by synoptically driven winds due to the relatively exposed location of the UFS (not shown). Only at GAP, Felsenkanzel, and ZPLT, the wind directions exhibited pronounced diurnal patterns that indicated thermally induced mountain winds, especially in summer (Fig. 4). However, the wind data from Felsenkanzel were not used because of problems with shifts of the sensor orientation. Upvalley and downvalley winds were characterized by northeasterly and southwesterly wind direction sectors at GAP, respectively, and by easterly and westsouthwesterly wind direction sectors at the ZPLT, respectively (Fig. 4). The wind patterns at the ZPLT were consistent with the study of Gantner et al. (2003) who observed a thermal circulation above the same plateau with an easterly inflow of a few hundred meters depth in the daytime and a westerly outflow at night under fair weather conditions in summer. Modeling suggested that the inflow ascended the narrow and deep valley Reintal before reaching the ZPLT.

The wind direction sectors at the ZPLT and GAP were used as a criterion for anabatic and katabatic winds (Table 2). Additionally, anabatic and katabatic winds were restricted to cases with a weak static stability ($\Delta\theta_v < 8$ K) and a strong static stability ($\Delta\theta_v \geq 8$ K), respectively, which was justified by the intersect between the frequency distributions of $\Delta\theta_v$ for the wind direction sectors described above (see supplement, Fig. S1b). For katabatic winds, a low wind velocity of $< 3\,m\,s^{-1}$ was

required at the ZPLT and GAP to exclude cases with a strong synoptic forcing. Additionally, both anabatic and katabatic winds were required to persist for at least 1 h, i.e. two time intervals (Table 2).

The detection of these winds and the ceilometer-based MLH at GAP were combined by a mechanistic approach that primarily accounted for thermally induced vertical transport. For this purpose, the $\mathrm{MLH_{GAP}}$ was discarded if clouds were detected at a height of $< 4 \, \mathrm{km \, a.s.l.}$ because low-level clouds increase the uncertainty of the MLH retrieval. The mechanistic approach distinguished between the following three conditions: (a) Anabatic winds occur or the UFS is below $\mathrm{MLH_{GAP}}$, which suggests BL air masses; (b) Katabatic winds occur and the UFS is above $\mathrm{MLH_{GAP}}$, which suggests UFT/SIN or HYBRID air masses; (c) The UFS is above $\mathrm{MLH_{GAP}}$ and the winds are not thermally induced, which also suggests UFT/SIN or HYBRID air masses under the assumption of identical MLHs at the UFS and GAP. This approach was limited by the low availability of the MLH (22 % after discarding times with low-level clouds) but still allowed for a partial verification of the statistical approach.

3 Results and discussion

3.1 Principal components and their seasonal dependence

The PCA converts several input variables into the same number of PCs while the variance and thus the importance of the PCs is highest for the first few PCs. In the winter half year, the percentage of explained variance of the PCs decreased strongly from PC1 to PC2 and more slightly towards higher-order PCs. In the summer half year, the explained variance decreased approximately linearly with increasing PC number (Fig. 5). The first two PCs explained a total of 60 % to 72 % and 53 % to 58 % of the variance in the winter half year and summer half year, respectively. Hence, most of the variance was maintained when reducing the number of considered PCs from six or seven to two, especially in the winter half year.

The loadings of the first two PCs were similar among the 2-month periods of the winter half year but different and more variable in the summer half year (Fig. 6). Although the loadings differed between the 2-month periods, PC1 was always a meaningful indicator for air mass classification, which will be explained in the following. PC2, as well as higher-order PCs, did not always allow for an unambiguous interpretation.

According to Eq. 5, variables with a high absolute loading determine the PC scores, i.e. the linear combinations, to a large extent. If, for example, an original variable is much higher than its 2-month mean value and its loading on PC1 is strongly negative then the variable will strongly contribute to a large negative score of PC1. In the winter half year, large negative scores of PC1 primarily reflected high CO, CO_2, and CH_4 mixing ratios and rather low values of $\Delta\theta_v$ (i.e. rather low static stability) and the air pressure at GAP (p_{GAP}), which suggested an uplift of BL air masses, while large positive scores of PC1 reflected the opposite characteristics suggesting a subsidence of UFT/SIN air masses (Fig. 6). PC2 primarily separated air masses with low q, high O_3, and rather high CH_4 mixing ratios from air masses with opposite characteristics in the winter half year. On its own, PC2 was a less reliable indicator for vertical transport because low q and high O_3 mixing ratios suggested a subsidence of UFT/SIN air masses while high CH_4 mixing ratios suggested an uplift of BL air masses. Possibly, PC2 reflects not only vertical but also horizontal concentration gradients.

In the summer half year, the loading of CO_2 on PC1 had the opposite sign compared to the loadings of CH_4 and CO on PC1. This observation suggests that low CO_2 mixing ratios were generally indicative for BL air masses during the vegetation period due to the CO_2 removal by photosynthesis. Additionally, p_{GAP} contributed more strongly to the first two PCs than in the winter half year and was anti-correlated with q. $\Delta\theta_v$ exhibited very small absolute loadings on the first two PCs in the periods April–May and June–July, indicating a poor correlation with the other variables.

In April and May, an uplift of BL air masses was indicated by large negative scores of PC1, which primarily reflected high q, low CO_2 mixing ratios, and low p_{GAP}, and by large negative scores of PC2, which primarily reflected high CO and CH_4 mixing ratios.

In June and July, PC1 separated cases with high CH_4, low CO_2, and low p_{GAP}, which indicated an uplift of BL air masses, from cases with opposite characteristics, which indicated a subsidence of UFT/SIN air masses. In the same period, PC2 could not be interpreted unambiguously with respect to vertical transport because high CO mixing ratios, which suggested BL air masses, but also low q and high p_{GAP}, which suggested UFT/SIN air masses, contributed to large negative scores of PC2.

In August and September, PC1 separated cases with high CO and CH_4 and low CO_2 and $\Delta\theta_v$ (i.e. low static stability), which was typical for BL air masses, from cases with opposite characteristics, which was typical for UFT/SIN air masses. Again, PC2 was a less reliable air mass indicator because low p_{GAP} and high q, which suggested an uplift of BL air masses, but also high CO_2 mixing ratios, which were typical for UFT/SIN air masses, increased the scores of PC2 in August and September (Fig. 6).

3.2 Air mass regimes in February and March

The interpretation of the air mass regimes, which were confined by the 33.3 % and 66.6 % percentiles of the first two PCs, differed among the 2-month periods except for the periods December–January and February–March. As an example, the period February–March is discussed in detail using summary statistics. A case study illustrating the classification results in the measured time series is shown in the supplement Sect. S3. The joint data availability of the PCA input variables was 87 % of the time in February–March.

For the regimes I, II, and III, the summary statistics of all seven PCA input variables were consistent with a recent uplift of BL air masses (Fig. 7a–g): Compared to the other regimes, CO, CH_4, and CO_2 generally exhibited high mixing ratios and q was also relatively high while O_3 and p_{GAP} were low or intermediate. $\Delta\theta_v$ indicated a weakly stable stratification with a median of approximately 8 K for the regimes I to III.

The other chemical and meteorological measurements supported the interpretation of the regimes I to III (Fig. 7h–r). Relatively high values for rH (medians between 80 % and 90 %) and total precipitation were consistent with a current uplift of air masses. For NO_y and NO_x, local pollution events ($\sigma_{NO_x} > 0.4$ ppb) were excluded while for ^{7}Be, N_{90}, eBC, and PM_{10}, cases with precipitation at the ZPLT were excluded from the summary statistics because local emissions or wet deposition obscure the chemical signature resulting from vertical transport processes. Nevertheless, the data availability of these variables was 75 % to 78 % of the time. The regimes I to III exhibited high NO_y, NO_x, and ^{222}Rn and low ^{7}Be concentrations compared to the other regimes, which underlines the strong influence of the BL. The high NO_x mixing ratios suggest a strong influence

12

of combustion processes. High ^{222}Rn concentrations are typical for the continental BL because of natural emissions from the ice-free land surface (Griffiths et al., 2014). ^{7}Be concentrations are generally low in the BL due to the formation by cosmic rays in the stratosphere and upper troposphere (Stohl et al., 2000). The aerosol concentrations N_{90}, eBC, and PM_{10} were somewhat elevated for the regimes I to III but not as strongly as the gas-phase measurements. This finding could be due to wet deposition during the uplift of the air masses. At ZSG, southeasterly to southerly winds with varying velocities were frequently observed for the three regimes under consideration (see supplement, Fig. S2a,d,g). The observations suggest that the influence of BL air masses was mostly caused by low pressure systems or south foehn events in February and March.

The regimes IV, V, and VI exhibited intermediate CO, CH_4, and CO_2 mixing ratios and an intermediate p_{GAP} (Fig. 7a–g). For these air masses, vertical transport processes were not inferable but the intermediate mixing ratios suggest an influence from both the BL and the free troposphere. Thus, the three regimes under consideration were attributed to the air mass class HYBRID, which was in line with intermediate NO_y, NO_x, and ^{222}Rn concentrations (Fig. 7l–n).

Regime VII was generally characterized by the lowest CO, CH_4, and CO_2 mixing ratios and a strongly stable stratification (median $\Delta\theta_v$ of 15 K). However, low O_3 mixing ratios, high q, and an intermediate and strongly variable p_{GAP} indicated that the air masses did not originate from the upper troposphere or stratosphere but from the lower troposphere or the marine boundary layer (Fig. 7a–g). This interpretation was in line with intermediate ^{7}Be and ^{222}Rn concentrations and low NO_y, NO_x, N_{90}, eBC, and PM_{10} concentrations (Fig. 7l–r). Intermediate rH with a median of 54 % corroborated some recent influence of the free troposphere. The air temperature was high compared to the other regimes (Fig. 7i), the wind direction at ZSG almost always had a south component, and the wind velocity at ZSG showed the highest mean of $10.22\,\mathrm{m\,s^{-1}}$ among the regimes (see supplement, Fig. S2c). The summary statistics did not allow for drawing a final conclusion on the influence of the marine boundary layer and thus, regime VII was attributed to the air mass class HYBRID and the subclass MBL/UFT unless the criteria for LRMD were fulfilled.

Balzani Lööv et al. (2008) clustered back-trajectories for the Jungfraujoch, another mountain site in the Alps, and demonstrated that some air masses originated from the marine boundary layer above the tropical Atlantic Ocean and were transported to the Jungfraujoch inside the free troposphere within 5 to 15 days, resulting in rather high rH (average of 67 %), high temperatures, and low O_3, CO, NO_y, and NO_x mixing ratios. Air masses with similar trajectories may also reach Mt. Zugspitze and represent, at least partly, the regime VII.

For the regimes VIII and IX, the CO, CH_4, and CO_2 mixing ratios were generally low but not as low as for regime VII. O_3 was intermediate for regime VIII and high for regime IX. Together with a strongly positive $\Delta\theta_v$ (median of approximately 15 K), i.e. a strongly stable stratification, and a generally high p_{GAP}, these observations indicated a subsidence of UFT/SIN air masses for the two regimes under consideration unless the criteria for LRMD were fulfilled (Fig. 7a–g). This interpretation was supported by a generally low rH (medians of 45 % and 25 %), a total precipitation of almost zero, low NO_y, NO_x, N_{90}, eBC, and PM_{10} concentrations, and high ^{7}Be concentrations compared to the other regimes (Fig. 7h–r).

For all regimes except III, the boxplots of global radiation (R_g) were similar with medians close to zero (Fig. 7k), indicating that the air mass characteristics were generally independent from day- and nighttime in February and March.

3.3 Seasonal frequencies of the air mass classes

In the entire year, the data availability limited the percentage of classified cases to 78% of the time. Data gaps occurred predominantly in the periods June–July and October–November (Fig. 8). On average, BL, UFT/SIN, and HYBRID air masses accounted for 31 %, 14 %, and 55 % of the classified cases, respectively. The percentage of UFT/SIN air masses is in reasonable agreement with the study of Yuan et al. (2019), in which 13.6 % of the long-term CO_2 data from the UFS were selected as baseline concentrations using an univariate statistical approach called "adaptive diurnal minimum variation selection". For earlier CO_2 data from ZSG and a pedestrian tunnel, approximately 70 m above the UFS, the percentage of baseline concentrations was 19.5 % and 9.9 %, respectively, according to the same study.

The air mass class BL was attributable to three of the nine air mass regimes in all 2-month periods except June–July and October–November when the class BL comprised two regimes (Fig. 8). This finding implies that air masses are lifted up to the UFS with similar frequencies in all seasons although the underlying processes may vary. However, the frequency of the air mass classes was constrained to some extent by using the 33.3 % and 66.6 % percentiles of the first two PCs as thresholds between the air mass regimes. These percentiles were somewhat arbitrary but allowed for a distinction between more unambiguous air masses at both edges of the distribution and more ambiguous air masses in the middle part of the distribution.

UFT/SIN air masses were attributable to two regimes in the winter half year but only to one regime in the period August–September and to none of the regimes in the periods April–May and June–July. UFT/SIN air masses were only evident if the summary statistics of an air mass regime indicated a dominating influence of subsidence. From April to July, subsidence appeared to be very rare at the UFS so that UFT/SIN air masses could not be isolated by splitting the data at the 33.3 % and 66.6 % percentiles of the first two PCs. This result can be explained by the fact that subsidence in high-pressure systems is counteracted by thermally induced uplift in the daytime, especially in the summer half year. However, the data availability in June–July was only 56 %, which questions the long-term representativeness for this period. Other statistical classifications at the high-alpine sites Jungfraujoch and Mt. Bachelor Observatory indicated that air masses of the undisturbed free troposphere occur year-round but less frequently in summer than in winter (Herrmann et al., 2015; Ambrose et al., 2011). In principle, these air masses do not have to descend but can also be advected horizontally to high-alpine sites. Such cases may be included in the class HYBRID and most likely in the subclass MBL/UFT.

HYBRID air masses including MBL/UFT comprised four to five regimes from August to March and even six and seven regimes in the periods April–May and June–July, respectively. In most of the 2-month periods, MBL/UFT air masses accounted for one regime (Fig. 8). Seven LRMD events were identified in the whole year, predominantly from April to July, which is in line with the study of Flentje et al. (2015) that found 5 to 15 Sahara dust events per year at the mountain site Hohenpeissenberg, approximately 40 km north of Mt. Zugspitze.

3.4 Comparing the statistical and mechanistic classifications

The ceilometer-based MLH at GAP exhibited a pronounced diurnal cycle with a maximum in the late afternoon or early evening on days with a high total global radiation (not shown). Little diurnal variations of the MLH were observed for days with a low

total global radiation. Thermally induced anabatic winds were most frequently observed during summer and daytime whereas thermally induced katabatic winds occurred most frequently at night and in the first few hours after sunrise (not shown). The patterns described above were expected and confirmed the plausibility of the mechanistic approach.

25 % of the statistically classified cases were evaluated with the mechanistic approach. In 3 % of the statistically classified cases, the mechanistic approach suggested an influence of the local BL on the UFS, mostly due to thermally induced anabatic winds. It should be noted that the mechanistic approach is not able to detect synoptic uplift processes because low-level clouds and precipitation result in data gaps of the MLH_{GAP}. In 5 % of the statistically classified cases, katabatic winds and a low MLH_{GAP} compared to the UFS level suggested non-BL air masses. In another 17 % of the statistically classified cases, the winds were not thermally induced and the MLH_{GAP} suggested non-BL air masses.

When the mechanistic approach suggested BL air masses, the statistical approach agreed in 56 % of the cases and yielded HYBRID air masses in almost all other cases (Fig. 9). This finding indicates a poor performance of the statistical approach in the case of thermally induced uplift. On the other hand, thermally induced uplift only accounts for a small fraction of the time according to the mechanistic approach. Other uplift processes including non-local uplift were not identifiable with the applied mechanistic approach. LRMD was found in 3 % of the cases, which were mechanistically classified as influenced by the BL, likely due to an overestimation of the ceilometer-based MLH_{GAP} if the advected dust layer merged with the mixing layer.

In the presence of katabatic winds and a low MLH_{GAP} compared to the UFS level, the statistical classes UFT/SIN and HYBRID including LRMD and MBL/UFT were both considered to agree with the mechanistic approach (illustrated by the thick black line in Fig. 9). Thus, the level of agreement was 91 % for katabatic winds and a relatively low MLH_{GAP}, whereby UFT/SIN and HYBRID air masses accounted for approximately half of these cases, respectively. When the MLH_{GAP} was lower than the UFS level and the winds were not thermally induced, the level of agreement between the classifications was a bit lower (86 %) with UFT/SIN and HYBRID air masses accounting for 34 % and 52 %, respectively.

Uncertainties of the mechanistic approach arise mainly from the assumption of identical MLHs at the UFS and GAP and the lack of information on non-local uplift followed by horizontal advection of air masses. Uncertainties of the statistical approach result primarily from the lack of objective thresholds between the air mass classes and a varying significance of sources and sinks of the gases used. In view of these uncertainties, a reasonable agreement between the approaches was found when the mechanistic approach indicated non-BL air masses.

3.5 Implications for real-time operational mode

To classify air masses in real-time, the scores of the first two PCs can be approximated by using the loadings that were calculated in this study. Thus, the same thresholds as described here can be applied to determine the regime and the class of the current air mass. To standardize the original variables, the arithmetic mean and standard deviation of the current 2-month period are required but these statistics are only known at the end of the 2-month period. Due to the long-term trends of CO_2, CH_4, and CO and the interannual variability of all variables, it is advisable not to use the 2-month means and standard deviations from the year investigated in the present study but to estimate these statistics from recent multi-year records. To make use of the known part of the current 2-month period, the mean (μ) and standard deviation (σ) could be updated regularly using weighted

averages,

$$\mu = (1-f)\mu_l + f\mu_c \tag{6}$$

$$\sigma = (1-f)\sigma_l + f\sigma_c \, , \tag{7}$$

where μ_l and σ_l are the 2-month mean and standard deviation, respectively, estimated from the long-term record, μ_c and σ_c are the mean and standard deviation of the known part of the current 2-month period, and f is the time fraction that is known in the current 2-month period. In real-time operational mode, additional uncertainties can arise from uncorrected measurement artifacts.

4 Conclusions

In this study, a novel statistical approach was developed to distinguish between the air mass classes BL (recent contact with the boundary layer), UFT/SIN (undisturbed free troposphere or stratospheric intrusion), and HYBRID (influences of both the boundary layer and the free troposphere or ambiguous characteristics) at the Schneefernerhaus at Mt. Zugspitze. A main purpose of the classification scheme is a later use in real-time operational mode. The scheme was based on the first two principal components, which were calculated from five gas-phase (CO, CH_4, CO_2, O_3, q) and two meteorological ($\Delta\theta_v$, p_{GAP}) variables but the principal components and their interpretation differed between the six 2-month periods. Additionally, the PM_{10} concentration and its 30 min standard deviation were needed to identify long-range transport of mineral dust. In retrospect, local pollution events on the mountain were evident from a high 30 min standard deviation of NO_x in approximately 9 % of the time. But these events are too short to be predictable on a 30 min basis in real-time applications and are thus neglected by the classification scheme.

While the first principal component was a suitable air mass indicator throughout the year, the second principal component left room for ambiguities. BL air masses were detected in all seasons with similar frequencies (average of 31 % of the classified cases). UFT/SIN air masses were predominantly found in the winter half year (23 % of the classified cases from October to March) but subsidence was so rare from April to July that the class UFT/SIN was not determinable in these months. HYBRID air masses (average of 55 % of the classified cases) mostly exhibited intermediate characteristics leaving room for ambiguities. For 17 % of HYBRID, it remained unclear whether the air mass originated from the lower undisturbed free troposphere or the marine boundary layer. To achieve a distinction between these two areas of origin, future work with trajectory models is necessary. 5 % of HYBRID was explained by long-range transport of mineral dust.

Independent chemical and standard meteorological measurements such as NO_y, ^{222}Rn, and precipitation were in line with the statistical approach. A mechanistic classification based on ceilometer and standard meteorological measurements was feasible in 25 % of the statistically classified cases and predominantly suggested non-BL air masses in these cases, which was in good agreement with the statistical approach. In the rare cases of thermally induced uplift, however, the statistical approach often misclassified BL air masses as HYBRID.

In principle, the statistical classification scheme can be used in real-time operational mode if the unknown arithmetic means and standard deviations of the observational variables in the current 2-month period can be estimated with sufficient accuracy. Future work should test the real-time applicability and quantify the uncertainty arising from the use of approximated means and standard deviations for standardization.

5   The framework of the presented statistical classification might also be useful at other high-alpine sites because it is based on common measurements.

References

Ambrose, J., Reidmiller, D., and Jaffe, D.: Causes of high O_3 in the lower free troposphere over the Pacific Northwest as observed at the Mt. Bachelor Observatory, Atmospheric Environment, 45, 5302 – 5315, https://doi.org/https://doi.org/10.1016/j.atmosenv.2011.06.056, 2011.

Balzani Lööv, J. M., Henne, S., Legreid, G., Staehelin, J., Reimann, S., Prévôt, A. S. H., Steinbacher, M., and Vollmer, M. K.: Estimation of background concentrations of trace gases at the Swiss Alpine site Jungfraujoch (3580 m asl), Journal of Geophysical Research: Atmospheres, 113, D22 305, https://doi.org/10.1029/2007JD009751, 2008.

Birmili, W., Weinhold, K., Rasch, F., Sonntag, A., Sun, J., Merkel, M., Wiedensohler, A., Bastian, S., Schladitz, A., Löschau, G., Cyrys, J., Pitz, M., Gu, J., Kusch, T., Flentje, H., Quass, U., Kaminski, H., Kuhlbusch, T. A. J., Meinhardt, F., Schwerin, A., Bath, O., Ries, L., Gerwig, H., Wirtz, K., and Fiebig, M.: Long-term observations of tropospheric particle number size distributions and equivalent black carbon mass concentrations in the German Ultrafine Aerosol Network (GUAN), Earth System Science Data, 8, 355–382, https://doi.org/10.5194/essd-8-355-2016, 2016.

Calvert, J. G.: Glossary of atmospheric chemistry terms (Recommendations 1990), Pure and Applied Chemistry, 62, 2167–2219, 1990.

Flentje, H., Heese, B., Reichardt, J., and Thomas, W.: Aerosol profiling using the ceilometer network of the German Meteorological Service, Atmospheric Measurement Techniques Discussions, 3, 3643–3673, https://doi.org/10.5194/amtd-3-3643-2010, 2010.

Flentje, H., Briel, B., Beck, C., Coen, M. C., Fricke, M., Cyrys, J., Gu, J., Pitz, M., and Thomas, W.: Identification and monitoring of Saharan dust: An inventory representative for south Germany since 1997, Atmospheric Environment, 109, 87 – 96, https://doi.org/https://doi.org/10.1016/j.atmosenv.2015.02.023, 2015.

Foken, T.: Micrometeorology, Springer, Berlin, Heidelberg, 2008.

Gallagher, J. P., McKendry, I. G., Cottle, P. W., Macdonald, A. M., Leaitch, W. R., and Strawbridge, K.: Application of Lidar Data to Assist Airmass Discrimination at the Whistler Mountaintop Observatory, Journal of Applied Meteorology and Climatology, 51, 1733–1739, https://doi.org/10.1175/JAMC-D-12-067.1, 2012.

Gantner, L., Hornsteiner, M., Egger, J., and Hartjenstein, G.: The diurnal circulation of Zugspitzplatt: observations and modeling, Meteorologische Zeitschrift, 12, 95–102, https://doi.org/doi:10.1127/0941-2948/2003/0012-0095, 2003.

Gohm, A., Harnisch, F., Vergeiner, J., Obleitner, F., Schnitzhofer, R., Hansel, A., Fix, A., Neininger, B., Emeis, S., and Schäfer, K.: Air Pollution Transport in an Alpine Valley: Results From Airborne and Ground-Based Observations, Boundary-Layer Meteorology, 131, 441–463, https://doi.org/10.1007/s10546-009-9371-9, 2009.

Griffiths, A. D., Conen, F., Weingartner, E., Zimmermann, L., Chambers, S. D., Williams, A. G., and Steinbacher, M.: Surface-to-mountaintop transport characterised by radon observations at the Jungfraujoch, Atmospheric Chemistry and Physics, 14, 12 763–12 779, https://doi.org/10.5194/acp-14-12763-2014, 2014.

Heese, B., Flentje, H., Althausen, D., Ansmann, A., and Frey, S.: Ceilometer lidar comparison: backscatter coefficient retrieval and signal-to-noise ratio determination, Atmospheric Measurement Techniques, 3, 1763–1770, https://doi.org/10.5194/amt-3-1763-2010, 2010.

Henne, S., Furger, M., Nyeki, S., Steinbacher, M., Neininger, B., de Wekker, S. F. J., Dommen, J., Spichtinger, N., Stohl, A., and Prévôt, A. S. H.: Quantification of topographic venting of boundary layer air to the free troposphere, Atmospheric Chemistry and Physics, 4, 497–509, https://doi.org/10.5194/acp-4-497-2004, 2004.

Herrmann, E., Weingartner, E., Henne, S., Vuilleumier, L., Bukowiecki, N., Steinbacher, M., Conen, F., Collaud Coen, M., Hammer, E., Juráñyi, Z., Baltensperger, U., and Gysel, M.: Analysis of long-term aerosol size distribution data from Jungfraujoch with emphasis on

free tropospheric conditions, cloud influence, and air mass transport, Journal of Geophysical Research: Atmospheres, 120, 9459–9480, https://doi.org/10.1002/2015JD023660, 2015JD023660, 2015.

Hulin, M., Gheusi, F., Lothon, M., Pont, V., Lohou, F., Ramonet, M., Delmotte, M., Derrien, S., Athier, G., Meyerfeld, Y., Bezombes, Y., Augustin, P., and Ravetta, F.: Observations of Thermally Driven Circulations in the Pyrenees: Comparison of Detection Methods and Impact on Atmospheric Composition Measured at a Mountaintop, Journal of Applied Meteorology and Climatology, 58, 717–740, https://doi.org/10.1175/JAMC-D-17-0268.1, 2019.

Kaiser, A., Scheifinger, H., Spangl, W., Weiss, A., Gilge, S., Fricke, W., Ries, L., Cemas, D., and Jesenovec, B.: Transport of nitrogen oxides, carbon monoxide and ozone to the Alpine Global Atmosphere Watch stations Jungfraujoch (Switzerland), Zugspitze and Hohenpeissenberg (Germany), Sonnblick (Austria) and Mt. Krvavec (Slovenia), Atmospheric Environment, 41, 9273 – 9287, https://doi.org/https://doi.org/10.1016/j.atmosenv.2007.09.027, 2007.

Ketterer, C., Zieger, P., Bukowiecki, N., Collaud Coen, M., Maier, O., Ruffieux, D., and Weingartner, E.: Investigation of the Planetary Boundary Layer in the Swiss Alps Using Remote Sensing and In Situ Measurements, Boundary-Layer Meteorology, 151, 317–334, https://doi.org/10.1007/s10546-013-9897-8, 2014.

Kirchner, M., Jakobi, G., Körner, W., Levy, W., Moche, W., Niedermoser, B., Schaub, M., Ries, L., Weiss, P., Antritter, F., Fischer, N., Henkelmann, B., and Schramm, K.-W.: Ambient Air Levels of Organochlorine Pesticides at Three High Alpine Monitoring Stations: Trends and Dependencies on Geographical Origin, Aerosol and Air Quality Research, 16, 738–751, https://doi.org/10.4209/aaqr.2015.04.0213, 2016.

Leuchner, M., Ghasemifard, H., Lüpke, M., Ries, L., Schunk, C., and Menzel, A.: Seasonal and Diurnal Variation of Formaldehyde and its Meteorological Drivers at the GAW Site Zugspitze, Aerosol and Air Quality Research, 16, 801–815, https://doi.org/10.4209/aaqr.2015.05.0334, 2016.

Löffler, H.: Meteorologische Bodenmesstechnik (vormals: Instrumentenkunde), vol. 6 of *Leitfaden für die Ausbildung im Deutschen Wetterdienst*, Selbstverlag des Deutschen Wetterdienstes, Offenbach am Main, 3 edn., https://www.dwd.de/DE/leistungen/pbfb_verlag_leitfaeden/l_einzelbaende/leitfaden6.html, 2012.

Mardia, K., Kent, J., and Bibby, J.: Multivariate analysis, Probability and mathematical statistics, Academic Press, 1979.

McClure, C. D., Jaffe, D. A., and Gao, H.: Carbon Dioxide in the Free Troposphere and Boundary Layer at the Mt. Bachelor Observatory, Aerosol and Air Quality Research, 16, 717–728, https://doi.org/10.4209/aaqr.2015.05.0323, 2016.

Poltera, Y., Martucci, G., Collaud Coen, M., Hervo, M., Emmenegger, L., Henne, S., Brunner, D., and Haefele, A.: PathfinderTURB: an automatic boundary layer algorithm. Development, validation and application to study the impact on in situ measurements at the Jungfraujoch, Atmospheric Chemistry and Physics, 17, 10 051–10 070, https://doi.org/10.5194/acp-17-10051-2017, 2017.

Reuten, C., Steyn, D. G., and Allen, S. E.: Water tank studies of atmospheric boundary layer structure and air pollution transport in upslope flow systems, Journal of Geophysical Research: Atmospheres, 112, D11 114, https://doi.org/10.1029/2006JD008045, 2007.

Risius, S., Xu, H., Di Lorenzo, F., Xi, H., Siebert, H., Shaw, R. A., and Bodenschatz, E.: Schneefernerhaus as a mountain research station for clouds and turbulence, Atmospheric Measurement Techniques, 8, 3209–3218, https://doi.org/10.5194/amt-8-3209-2015, 2015.

Ruckstuhl, A. F., Henne, S., Reimann, S., Steinbacher, M., Vollmer, M. K., O'Doherty, S., Buchmann, B., and Hueglin, C.: Robust extraction of baseline signal of atmospheric trace species using local regression, Atmospheric Measurement Techniques, 5, 2613–2624, https://doi.org/10.5194/amt-5-2613-2012, 2012.

Schuster, C., Kirchner, M., Jakobi, G., and Menzel, A.: Frequency of inversions affects senescence phenology of Acer pseudoplatanus and Fagus sylvatica, International Journal of Biometeorology, 58, 485–498, https://doi.org/10.1007/s00484-013-0709-0, 2014.

Seibert, P., Beyrich, F., Gryning, S.-E., Joffre, S., Rasmussen, A., and Tercier, P.: Review and intercomparison of operational methods for the determination of the mixing height, Atmospheric Environment, 34, 1001–1027, https://doi.org/10.1016/S1352-2310(99)00349-0, 2000.

Steinkopff, T., Frank, G., and Salvamoser, J.: Measurement of radionuclides within the Global Atmosphere Watch Programme of WMO, Kerntechnik, 77, 193–196, 2012.

5   Stohl, A., Spichtinger-Rakowsky, N., Bonasoni, P., Feldmann, H., Memmesheimer, M., Scheel, H., Trickl, T., Hübener, S., Ringer, W., and Mandl, M.: The influence of stratospheric intrusions on alpine ozone concentrations, Atmospheric Environment, 34, 1323 – 1354, https://doi.org/https://doi.org/10.1016/S1352-2310(99)00320-9, 2000.

Stull, R. B.: An Introduction to Boundary Layer Meteorology, Kluwer Acad. Publ., Dordrecht, Boston, London, 1988.

Sun, J., Birmili, W., Hermann, M., Tuch, T., Weinhold, K., Spindler, G., Schladitz, A., Bastian, S., Löschau, G., Cyrys, J., Gu, J., Flentje,
10   H., Briel, B., Asbach, C., Kaminski, H., Ries, L., Sohmer, R., Gerwig, H., Wirtz, K., Meinhardt, F., Schwerin, A., Bath, O., Ma, N., and Wiedensohler, A.: Variability of Black Carbon Mass Concentrations, Sub-micrometer Particle Number Concentrations and Size Distributions: Results of the German Ultrafine Aerosol Network Ranging from City Street to High Alpine Locations, Atmospheric Environment, https://doi.org/https://doi.org/10.1016/j.atmosenv.2018.12.029, 2018.

WDCGG: World Data Centre for Greenhouse Gases, https://gaw.kishou.go.jp, last access: 2 February, 2019.

15   Young: Wind Monitor - Model 05103, http://www.youngusa.com/products/7/5.html, last access: 23 December, 2018.

Yuan, Y., Ries, L., Petermeier, H., Steinbacher, M., Gómez-Peláez, A. J., Leuenberger, M. C., Schumacher, M., Trickl, T., Couret, C., Meinhardt, F., and Menzel, A.: Adaptive selection of diurnal minimum variation: a statistical strategy to obtain representative atmospheric CO_2 data and its application to European elevated mountain stations, Atmospheric Measurement Techniques, 11, 1501–1514, https://doi.org/10.5194/amt-11-1501-2018, 2018.

20   Yuan, Y., Ries, L., Petermeier, H., Trickl, T., Leuchner, M., Couret, C., Sohmer, R., Meinhardt, F., and Menzel, A.: On the diurnal, weekly, and seasonal cycles and annual trends in atmospheric CO_2 at Mount Zugspitze, Germany, during 1981–2016, Atmospheric Chemistry and Physics, 19, 999–1012, https://doi.org/10.5194/acp-19-999-2019, 2019.

Zellweger, C., Forrer, J., Hofer, P., Nyeki, S., Schwarzenbach, B., Weingartner, E., Ammann, M., and Baltensperger, U.: Partitioning of reactive nitrogen (NO_y) and dependence on meteorological conditions in the lower free troposphere, Atmospheric Chemistry and Physics,
25   3, 779–796, https://doi.org/10.5194/acp-3-779-2003, 2003.

Zhang, L. and Jaffe, D. A.: Trends and sources of ozone and sub-micron aerosols at the Mt. Bachelor Observatory (MBO) during 2004-2015, Atmospheric Environment, 165, 143 – 154, https://doi.org/https://doi.org/10.1016/j.atmosenv.2017.06.042, 2017.
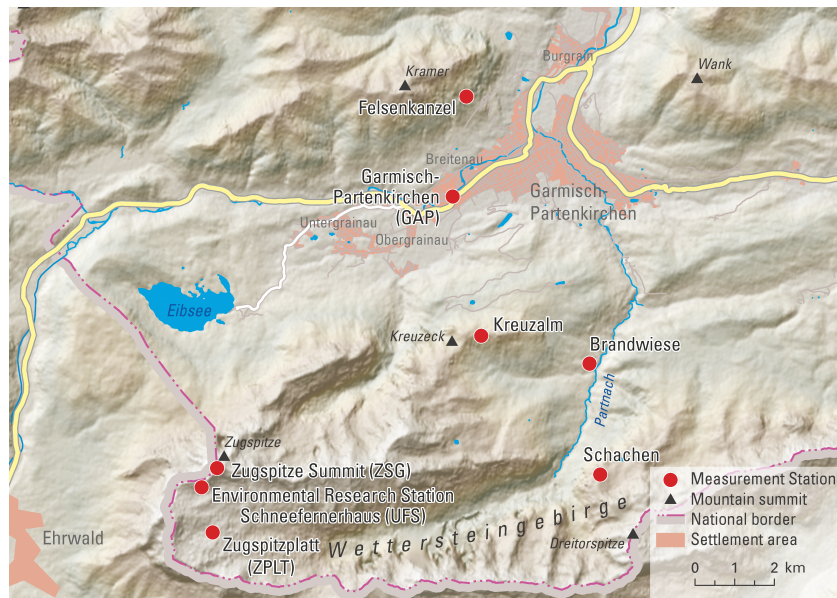
Figure 1. Location of the measurement sites in the surrounding of Mt. Zugspitze. North is at the top.
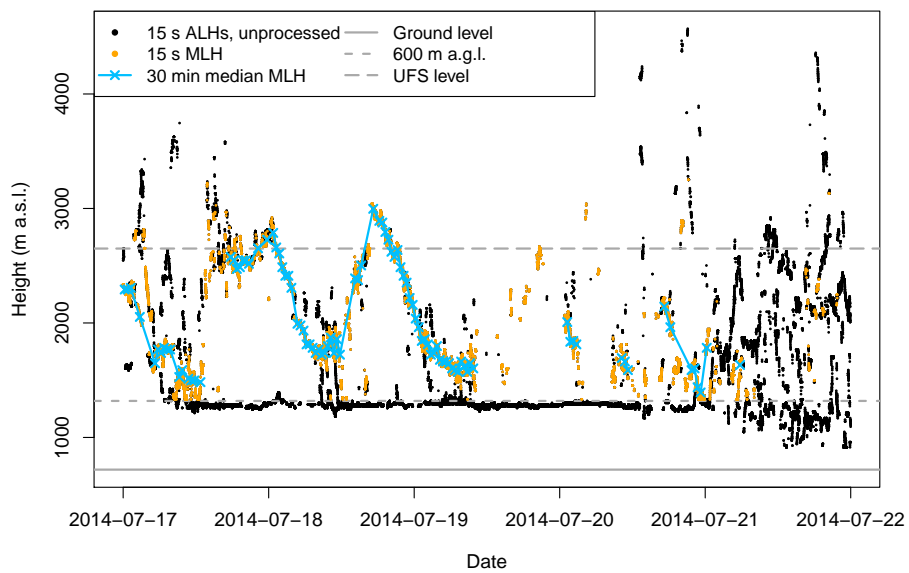
Figure 2. Post-processing of the ceilometer-based aerosol layer heights (ALHs), which were used to determine the mixing layer height (MLH) at GAP, illustrated for the period from 17 to 21 July 2014. From the MLH, outliers have been removed. Points of the 30 min median MLH were connected by a line if separated by maximum 3 h.
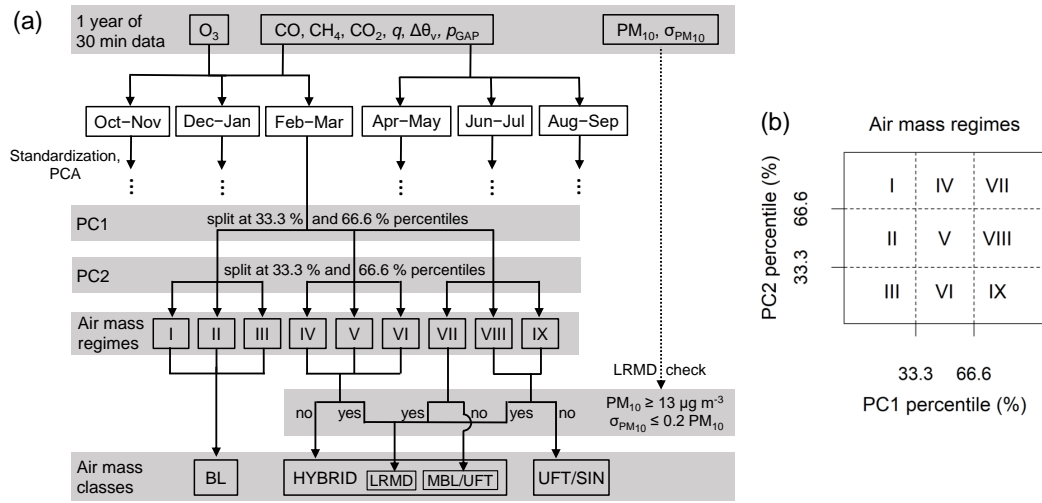
Figure 3. (a) Scheme for statistical air mass classification at the UFS using the first (PC1) and second principal components (PC2) of a 6- or 7-dimensional data set. The mapping of air mass regimes to air mass classes is only shown for February and March and was different for other 2-month periods. BL denotes a recent contact with the boundary layer, UFT/SIN includes the undisturbed free troposphere and stratospheric intrusions, and HYBRID reflects influences from both BL and UFT/SIN and includes the subclasses LRMD (long-range transport of mineral dust) and MBL/UFT (influence of the marine boundary layer or UFT). (b) Numbering of the air mass regimes.
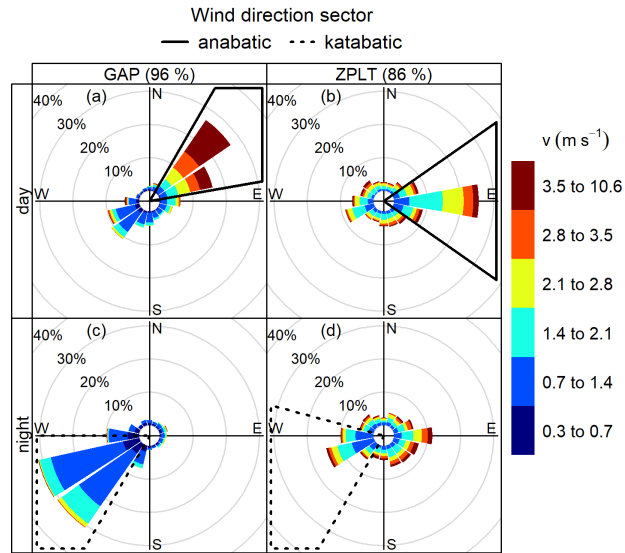
Figure 4. Wind rose plots showing the frequency of counts by wind direction and velocity (v) at the sites GAP (a,c) and ZPLT (b,d) during day- (a,b) and nighttime (c,d) in summer (June to August). Daytime was defined by a global radiation of $> 5 \, \mathrm{W \, m^{-2}}$ at minimum one of the sites used in this study; all other cases were treated as nighttime. The plots were used to define wind direction sectors for thermally induced anabatic and katabatic winds. The percentage in brackets specifies the data availability.
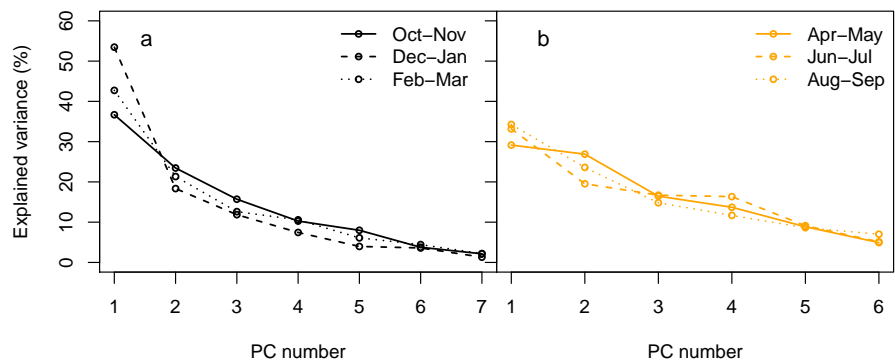
Figure 5. Percentage of explained variance as a function of the principal component (PC) number for each 2-month period: (a) winter half year and (b) summer half year.
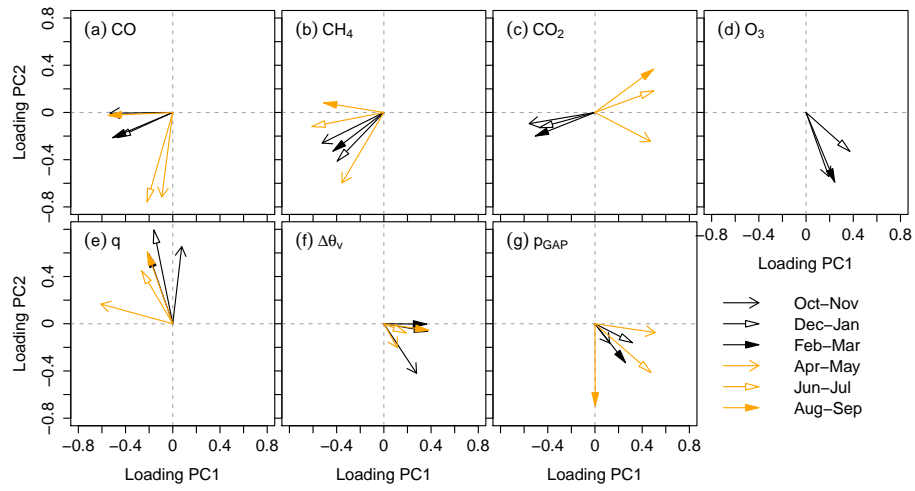
Figure 6. Loadings of the input variables on the first (PC1) and second principal component (PC2) for each 2-month period. O_3 was only used as an input variable in the winter half year (black arrows).
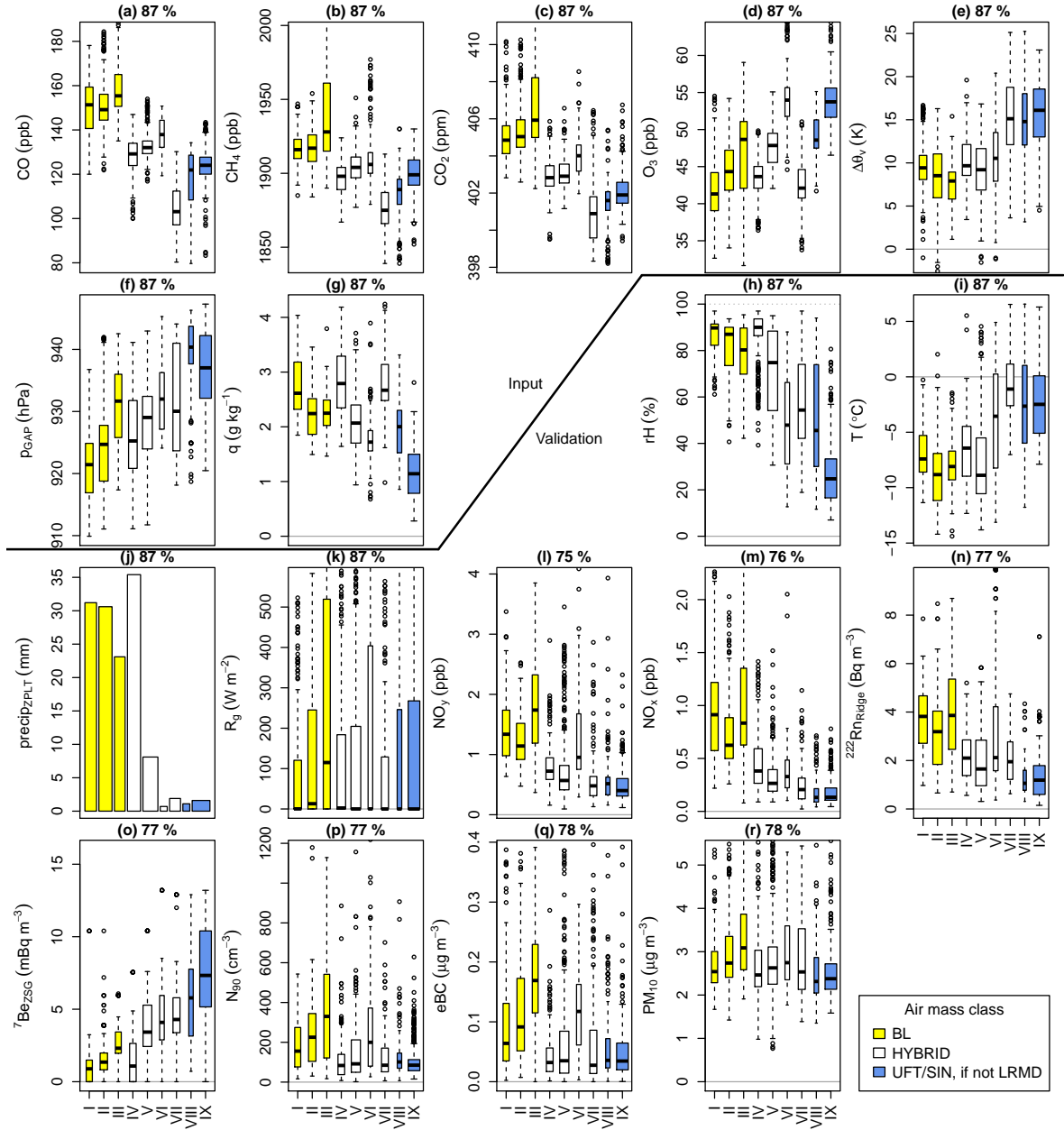
Figure 7. Summary statistics of PCA input variables (a–g) and validation variables (h–r) for the nine statistical air mass regimes in February and March 2014. The boxes show the quartiles and the boxwidth is proportional to the number of data points; each whisker is limited to a length of 1.5 times the interquartile range. Total precipitation ($precip_{ZPLT}$) is depicted in a bar plot. Unless labeled differently, the data was measured at the UFS except for $\Delta\theta_v$ that represents the maximum difference among the sites. Symbols are explained in Sect. 2.2 and 2.3. Above the plots, the data availability is specified as fraction of time. For NO_x and NO_y, local pollution events were excluded. For $^7Be_{ZSG}$, N_{90}, eBC, and PM_{10}, cases with precipitation ($precip_{ZPLT} > 0$) were excluded. The axis of ordinate was limited to $m \pm 3\,MAD$, where m and MAD are median and median absolute deviation of individual regimes, respectively.
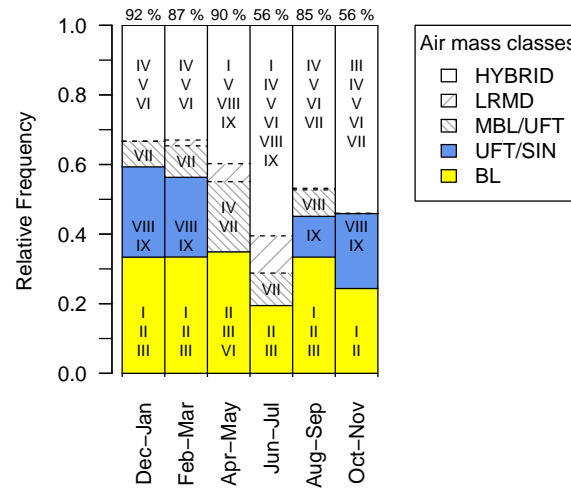
Figure 8. Relative frequency of the air mass classes as fraction of the classified cases in each 2-month period. Above the plot, the joint data availability is given as fraction of time. LRMD (long-range transport of mineral dust) represents certain cases within the regimes that were not attributed to BL (recent contact with the boundary layer). LRMD and MBL/UFT (influence of the marine boundary layer or UFT) are part of HYBRID (influences of both the boundary layer and the free troposphere or ambiguous). UFT/SIN denotes undisturbed free troposphere or stratospheric intrusion.
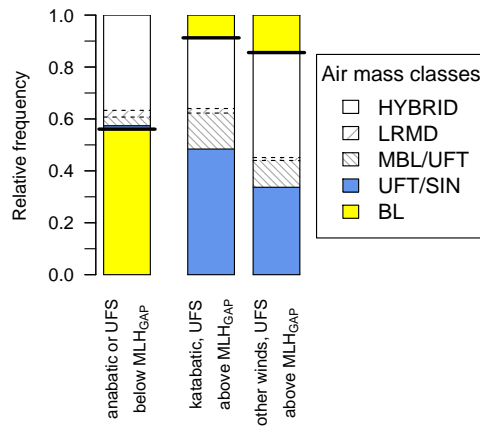
Figure 9. Comparison between the statistical and mechanistic classifications of air masses. The mechanistic classes were based on the boundary layer height at GAP (MLH_{GAP}) and thermally induced anabatic and katabatic winds (Sect. 2.5) and accounted for 3 %, 5 %, and 17 % of the statistically classified cases (from left to right). The thick black lines show the percentages considered as an agreement between the approaches. MLH_{GAP} was discarded if clouds were detected below 4 km a.s.l.. LRMD and MBL/UFT are subclasses of HYBRID.

Table 1. Chemical measurements used in this study. The given interval is the temporal interval at which the data were provided by the respective institution. UV denotes ultraviolet light. The symbols for the measured quantities are explained in the text.

Symbol	Instrument	Interval	Unit	Measurement principle	Institution
CO	AL5002, Aero-Laser, Garmisch-Partenkirchen, Germany	1 min	ppb	UV fluorescence	UBA[e]
CH_4	EnviroSense 3000i, PICARRO, Sunnyvale, USA	1 min[a]	ppb	cavity ringdown spectroscopy	UBA[e]
CO_2	EnviroSense 3000i, PICARRO, Sunnyvale, USA	1 min[a]	ppm	cavity ringdown spectroscopy	UBA[e]
O_3	Model 49i, Thermo Scientific, Waltham, USA	1 min	ppb	UV absorption	UBA[e]
NO_y, NO_x	CraNOx II, ECO PHYSICS, Dürnten, Switzerland	1 min	ppb	chemiluminescence	UBA[e]
HCHO	AL4021, Aero-Laser, Garmisch-Partenkirchen, Germany	10 min	ppb	fluorometric Hantzsch reaction[c]	TUM[f]
^{222}Rn	Radon sphere 270, IGU, Wörthsee, Germany	2 h	$Bq\,m^{-3}$	electrostatic deposition followed by alpha particle spectrometry[d]	DWD[g]
^7Be	Glass fiber filter and pump, Tracerlab, Köln, Germany	12 h	$mBq\,m^{-3}$	gamma spectrometry	DWD[g]
$dN\,(dlog\,d_p)^{-1}$	SMPS[b] model 3936, TSI Inc., Shoreview, USA	10 min	cm^{-3}	separation of charged particles in an electric field	TROPOS[h]
PM_{10}	FH 62 C14, Thermo Scientific, Waltham, USA	1 min	$\mu g\,m^{-3}$	attenuation of beta radiation	UBA[e]
eBC	MAAP[b] model 5012, Thermo Scientific, Waltham, USA	1 min	$\mu g\,m^{-3}$	light attenuation and reflection by particle-laden quartz fiber filters	UBA[e]

[a] 30 min in the year 2014; [b] see Birmili et al. (2016) and Sun et al. (2018) for details on the Scanning Mobility Particle Sizer (SMPS) and the Multi Angle Absorption Photometer (MAAP); [c] see Leuchner et al. (2016) for details; [d] see Steinkopff et al. (2012) for details; [e] German Environment Agency; [f] Ecoclimatology, Technical University of Munich; [g] German Meteorological Service; [h] Experimental Aerosol and Cloud Microphysics, Leibniz Institute for Tropospheric Research

Table 2. Criteria for thermally induced anabatic and katabatic winds occurring simultaneously at GAP and ZPLT. φ is wind direction, v is wind velocity, and $\Delta\theta_v$ is the range of the pseudo-vertical profile of virtual potential temperature.

Wind class	φ_{GAP}	φ_{ZPLT}	$\Delta\theta_v$	v_{ZPLT} and v_{GAP}	Duration
Anabatic	$30°$ to $80°$	$55°$ to $125°$	< 8 K		≥ 1 h
Katabatic	$210°$ to $270°$	$210°$ to $285°$	≥ 8 K	$< 3\,\mathrm{m\,s^{-1}}$	≥ 1 h